Dynamics and Metallicities of Red Supergiant Stars in the Young Massive Cluster NGC 2100

L. R. Patrick[1]⋆, C. J. Evans[1,2], B. Davies[3], et al.

[1] *Institute for Astronomy, University of Edinburgh, Royal Observatory Edinburgh, Blackford Hill, Edinburgh EH9 3HJ, UK*
[2] *UK Astronomy Technology Centre, Royal Observatory Edinburgh, Blackford Hill, Edinburgh EH9 3HJ, UK*
[3] *Astrophysics Research Institute, Liverpool John Moores University, Liverpool Science Park ic2, 146 Brownlow Hill, Liverpool L3 5RF, UK*

ABSTRACT

We have obtained KMOS near-IR spectroscopy for 14 red supergiant stars in the young massive star cluster NGC 2100 in the Large Magellanic Cloud (LMC). Radial velocities are estimated for the targets and the dynamical properties are estimated for the first time within this cluster. The line-of-sight velocity dispersion is shown to be flat outside of 10 pc from the cluster centre and is estimated to be $\sigma_{1D} = 3.4 \pm 0.5\,\mathrm{km\,s^{-1}}$. The dynamical mass of the cluster is derived as $M_{dyn} > (4.2 \pm 1.4) \times 10^4 M_{\odot}$ assuming virial equilibrium. Comparing this to the mass estimated using photometry we find reasonable agreement between the independent measurements, suggesting that the cluster is in virial equilibrium and that the the velocity dispersion is not increased by binary motions and has a normal IMF.

Stellar parameters including metallicity are estimated using the J-band analysis technique which has been rigorously tested in the Local Universe. We find an average metallicity for NGC 2100 at $-0.39 \pm 0.10\,dex$, in good agreement with estimates from the literature. The age of the NGC 2100 is estimated to be $20 \pm 5\,\mathrm{Myr}$ using isochrone fitting to the RSG population, also in good agreement with previous estimates.

Key words: Red Supegiants: stars. Clusters: NGC 2100. Galaxy: LMC.

1 INTRODUCTION

Young massive clusters (YMCs) are important probes of early cluster evolution and have increasingly been used as tracers of star formation in galaxies (e.g. Whitmore & Schweizer 1995; Miller et al. 1997; Zepf et al. 1999), where a YMC is defined as $< 100\,\mathrm{Myr}$ and $> 10^4\,\mathrm{M_{\odot}}$ (Portegies Zwart et al. 2010). Known to contain large populations of massive stars YMCs are also important tracers of massive star formation, which is heavily clustered (de Wit et al. 2005; Parker & Goodwin 2007). In addition to being the birthplace of most of the massive stars in the Local Universe ($> 200\,\mathrm{M_{\odot}}$ stars in R136 Crowther et al. 2010), owing to the density of stars, YMCs are also the birthplace of rich stellar exotic found in the old population of GCs (Portegies Zwart et al. 2010).

Establishing a link between YMCs and older GCs is an important, uncertain, factor in the evolution of young clusters. The vast majority of star formation occurs within a clustered environment (**?**) However, observations of stars in the disk of the Milky Way show that only a small fraction of stars are actually found with clusters today (). **This is true, but only about 10% of stars form in clusters in Milky Way type galaxies (see Adamo & Bastian 2015)** This indicates that a significant fraction of star clusters will dissolve over time.

Studying the dynamical properties of YMCs is an important tool to evaluate the likelihood that a young cluster will survive to become an old GC. The end of the process of star formation, brought about by the expulsion of the most massive stars in the cluster as supernovae, expels residual gas and leaves a young cluster in a super-virial state (i.e. unstable to dissolution Lada & Lada 2003). **no, they are gas free before the first SNe (Hollyhead et al. 2015). See also Longmore et al. (2014, PPVI review) for more discussions on the early dynamics of clusters** This is key period in determining the survival of a young star cluster. Observations that the some YMCs (namely R136 in the Large Magellanic Cloud) are in dynamical equilibrium from an early age (Hénault-Brunet et al. 2012; Longmore et al. 2014) challenges the view that star clusters expand owing to gas expulsion. An alternative explanation is that these clusters expand owing to stellar evolution on a slow timescale (compared to the cross time of the cluster 10 Myr Portegies Zwart et al. 2010) and hence remain in virial equilibrium. **the crossing time is much shorter for most**

⋆ E-mail: lrp@roe.ac.uk

of the clusters, around 1 Myr or less. Challenging this, (Banerjee & Kroupa 2013) suggested that the observation that YMCs are in dynamical equilibrium from an early age does not necessarily indicate that the cluster did not undergo a period of rapid gas expulsion implying that the cluster could quickly re-virialise on a short timescale.

Recently, the idea that globular clusters are simple stellar populations has been called into question based on their kinematics, metallicities and main sequence turn-offs. Studying young massive clusters could therefore potentially help to constrain some of the proposed models for creating multiple stellar populations within GCs.

Over the last few years, medium resolution ($R > 3000$) near-IR spectroscopy has been shown to be a powerful tool to estimate stellar parameters for red supergiant stars (RSGs; Davies et al. 2010). This technique has been tested rigorousness by Gazak et al. (2014) and Davies et al. (2015). The arrival of the K-band multi-object spectrograph (KMOS; Sharples et al. 2013) at the Very Large Telescope (VLT), has presented new opportunities for efficient observations of samples of RSGs in external galaxies to study their distribution and build-up of metals. Patrick et al. (2015) used KMOS observations to investigate present day metallicities of NGC 6822 (d = 0.5 Mpc) and Gazak et al. (2015) used KMOS to determine the metallicity gradient of NGC 300, a grand design spiral galaxy outside the Local Group ($d = 1.9\,Mpc$), finding striking agreement with blue supergiant stars (BSGs).

NGC 2100 is a young massive cluster in the LMC, located near the large star-forming region 30 Doradus. With an age of $\sim$20 Myr (Elson 1991; Niederhofer et al. 2015), and a mass of $4.6 \times 10^4 M_\odot$ (McLaughlin & van der Marel 2005, assuming King (1966) profiles), NGC 2100 falls within the mass and age range where the infrared cluster light is dominated by RSGs (Gazak et al. 2013), supported by the large number of RSGs identified within this cluster (e.g. Figure 1).

NGC 2100 is not a cluster in isolation. It is located in one of the most actively star-forming regions within the Local Group of galaxies. At $\sim$20 Myr old, the most massive members of this star cluster will have already exploded as supernovae. This will have a profound effect on the surrounding gas and dust, and has potentially shaped the surrounding LMC 2 supershell (see Points et al. 1999).

In this study we estimate stellar parameters from KMOS spectroscopy for 14 RSGs in the vicinity of the young massive cluster NGC 2100. Section 2 we describe the observations and data reduction, and in section 3 we detail our results, focusing on radial velocities of the target stars where we derive the line-of-sight velocity dispersion, the dynamical mass of NGC 2100 and the stellar parameters. Our results are discussed in Section 4 and conclusions are presented in Section 5.

2   OBSERVATIONS AND DATA REDUCTION

2.1   Target Selection

- Ben, could you write a few lines here?
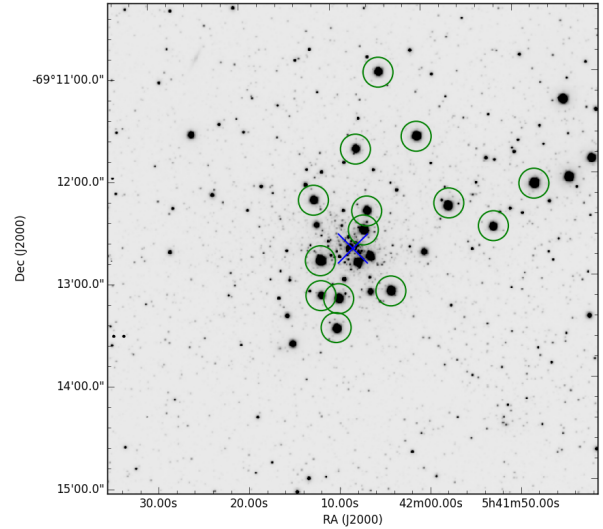
Figure 1. Positions of the NGC 2100 KMOS targets overlaid on a VISTA *J*-band image. Green circles indicate KMOS targets. The adopted cluster centre has been marked by a blue cross.

2.2   KMOS Observations

These observations were obtained as part of the KMOS Guaranteed Time Observing (PI: Evans) and were conducted in March 2015. The observations consisted of 8×10 s exposures taken with the YJ grating with sky offset exposures (S) interleaved between the object (O) exposures in an O, S, O observing pattern. In addition, a standard set of KMOS calibration frames were obtained as well as observations of HD 51506 (B5) as the telluric standard star. Seeing conditions were stable at 1.0 arcseconds for the course of the observations.

The KMOS/esorex standard routines (SPARK; Davies et al. 2013) were used to calibrate and reconstruct the data cubes. Telluric correction was performed using the 24-arm telluric correction routine (described in detail by Patrick et al. 2015). Briefly, corrections to the standard telluric recipe are put in place to correct for slight differences in wavelength calibration between the telluric and science spectra. This is implemented using an iterative cross-correlation approach. Additionally, differences in the strength of the telluric features are corrected by applying a simple scaling using the equation,

$$T_2 = (T_1 + c)/(1 + c) \qquad (1)$$

where T_2 is the scaled telluric-standard spectrum, T_1 is the uncorrected telluric-standard spectrum and c is the scaling parameter which is varied from $c = -0.5$ to $c = 0.5$ in increments of 0.02. The best c value is chosen based on the overall standard deviation of the spectrum, i.e. the c value producing the smallest σ is selected. Once these corrections are accounted for, the science spectra are divided by the appropriate telluric spectrum for that particular IFU.

Table 1. Summary of VLT-KMOS targets in NGC 2100.

ID	S/N	α (J2000)	δ (J2000)	B	V	I	J	H	K_{s}	RV (km s^{-1})	Notes
J054147.86-691205.9	318	05:41:47.873	-69:12:05.959	16.488	13.749	9.769	9.525	8.603	8.200	250.3 ±4.7	
J054152.51-691230.8	198	05:41:52.430	-69:12:30.410	16.430	14.267	11.970	10.413	9.526	9.155	249.3 ±2.6	
J054157.44-691218.1	202	05:41:57.286	-69:12:16.480	14.074	13.019	11.170	9.811	9.036	8.738	245.6 ±3.5	C2
J054203.90-691307.4	252	05:42:03.877	-69:13:07.410	15.624	13.579	11.410	9.839	8.996	8.740	251.1 ±2.8	
J054206.36-691220.2	196	05:42:06.348	-69:12:20.150	. . .	. . .	11.810	10.371	9.480	9.159	255.7 ±4.9	B17
J054206.77-691231.1	256	05:42:06.764	-69:12:31.245	15.643	13.675	11.390	9.977	9.150	8.807	250.6 ±3.4	
J054209.66-691311.2	240	05:42:09.647	-69:13:11.263	15.367	13.383	11.370	9.976	9.136	8.841	254.3 ±4.1	
J054209.98-691328.8	250	05:42:10.001	-69:13:28.210	16.060	13.827	11.580	10.021	9.150	8.823	250.2 ±3.0	C32
J054211.56-691248.7	304	05:42:11.574	-69:12:48.770	16.327	14.033	11.450	9.557	8.617	8.264	255.5 ±4.3	
J054211.61-691309.2	151	05:42:11.592	-69:13:09.257	16.165	14.272	12.340	10.943	10.090	9.788	256.6 ±6.1	
J054212.20-691213.3	195	05:42:12.182	-69:12:13.144	15.483	13.606	11.750	10.440	9.622	9.335	260.0 ±4.8	
J054200.74-691137.0	262	05:42:00.722	-69:11:36.925	15.579	13.674	9.421	9.900	9.017	8.683	248.8 ±2.7	
J054204.78-691058.8	211	05:42:04.762	-69:10:58.816	15.550	13.800	12.770	10.319	9.427	9.159	256.1 ±4.0	
J054207.45-691143.8	201	05:42:07.435	-69:11:43.692	15.531	13.661	11.780	10.482	9.610	9.351	252.5 ±3.0	

Photometric data taken from the SIMBAD database. Typical errors on photometric data: 0.026, 0.014, 0.04, 0.024, 0.026, 0.022 respectively. Near-IR data taken from 2MASS.

3 RESULTS

3.1 Radial velocities

Radial velocities are estimated using an iterative cross-correlation method. To ensure systematic shifts are removed, the observed spectra are first cross-correlated against a spectrum of the Earth's atmosphere, taken from the ISAAC webpages at a much higher resolution than that of the KMOS observations. This spectrum is then degraded to the resolution of the observations using a simple Gaussian filter. The cross-correlation is performed within the $1.140 - 1.1155\,\mu$m region as in this region a strong set of reliable telluric features dominate, with no contamination from stellar features. The shift arising from this region is typically between $0-10$ km s^{-1} and is then applied to the $1.16-1.22\,\mu$m region, i.e. where the radial velocity is estimated.

Once the observed spectra are on a consistent wavelength solution, an initial guess of the radial velocity is estimated by cross-correlating the science spectra with an appropriate synthetic RSG spectrum in the $1.17 - 1.21\,\mu$m region. This wavelength regime is selected based on the dominance of atomic features in the RSG spectrum at these wavelengths. To increase reliability, this initial guess is improved upon by using seven, independent, carefully selected strong stellar absorption lines which are chosen based on the strength of the line and the level of telluric contamination.

Radial velocities are independently calculated for each line by means of iterative cross-correlation. This results in seven estimates of the radial velocity for each star which are then compared. Any line which produces a radial velocity which is an obvious outlier to the distribution is rejected (i.e. several hundred km s^{-1} discrepant from the other values). This can occasionally be the case when the cross-correlation incorrectly centres on a local minimum, a simple visual inspection of the resulting spectra once the shift has been implemented is sufficient to remove these cases.

The final radial velocity for each star is the mean of the distribution resulting from the (non-rejected) lines, where the error on this mean is calculated by taking the standard deviation of the data, normalised by the number of regions used ($err = \sigma/N_{regions}$). This method is known to work well for KMOS spectra (Lapenna et al. 2015; Patrick et al. 2015).

Figure 2 shows all stellar radial velocity estimates as a function of distance from the centre of the cluster, alongside the systemic radial velocity of the LMC (green dashed line). Given the low dispersion of the radial velocity measurements for the KMOS targets, we confirm that all of the targets within this sample are members of NGC 2100. The average value of the sample is 251.5 ± 3.4 km s^{-1}. Below this average value is compared with previous measurements within the cluster and Table 2 details these previous measurements.

Recently, Evans et al. (2015) used AAOmega to measure radial velocities of massive stars within LMC, which included two sources in NGC 2100: star 407 (O9.5 II 258.5 ± 3.4 km s^{-1}) and star 408 (B3 Ia; 250.6 ± 1.3 km s^{-1}). Massive blue stars are known to preferentially reside within binary systems (Sana et al. 2012) which could increase their radial velocity measurements significantly (Hénault-Brunet et al. 2012). If these massive blue stars were in binaries we would expect the RSG radial velocities to be lower than the velocities measured in these stars. We find however, good agreement between our measurements and those from Evans et al. (2015), indicating that these two blue stars within NGC 2100 are not affected significantly by the effects of binary motions.

Jasniewicz & Thevenin (1994, henceforth JT94) measured radial velocities for four RSGs in NGC 2100 (B17, C2, C32 and C34, using the nomenclature of Robertson 1974). Three of these stars have been observed with KMOS in the present study (J054206.36-691220.2; B17, J054157.44-691218.1; C2 and J054209.98-691328.8; C32). The average offset between the three stars which are common to the samples is -11.2 ± 9.0 km s^{-1}, dominated by the difference in measurements from C2. However, when taken in context with other values in NGC 2100 the value of 270 ± 8 km s^{-1} appears to be an outlier. We conclude that there exists no significant offset between our measurements and previous estimates within NGC 2100.

Freeman et al. (1983) compiled integrated-light radial velocities from Andrews & Lloyd Evans (1972) and Ford (1970) to define an average of 267 ± 13 km s^{-1} for NGC 2100. Whereas Smith & Weedman (1971), measured the radial velocity of the HII gas of NGC 2100 as 282.2 ± 2.5 km s^{-1}.

Table 2. Previous radial velocity measurements in NGC 2100.

ID	ID in current study	RV (km s^{-1}) Lit.	RV (km s^{-1}) this study	Reference	Notes
407	—	258.5 ± 3.4	...	Evans et al. (2015)	O9.5 II
408	—	250.6 ± 1.3	...	Evans et al. (2015)	B3 Ia
B17	J054206.36-691220.2	255 ± 8	255.7 ± 4.9	Jasniewicz & Thevenin (1994)	
C2	J054157.44-691218.1	270 ± 8	245.6 ± 3.5	Jasniewicz & Thevenin (1994)	
C32	J054209.98-691328.8	260 ± 8	250.2 ± 3.0	Jasniewicz & Thevenin (1994)	
C34	—	265 ± 8	...	Jasniewicz & Thevenin (1994)	
NGC 2100	—	280 ± 10(16)	...	Andrews & Lloyd Evans (1972)	Whole cluster
NGC 2100	—	282.2 ± 2.5	...	Smith & Weedman (1971)	Gas
NGC 2100	—	253 ± 17	...	Ford (1970)	

Value in braces is the error defined from Freeman et al. (1983). First radial velocity column, the first value is from the literature and the second is determined in this work.
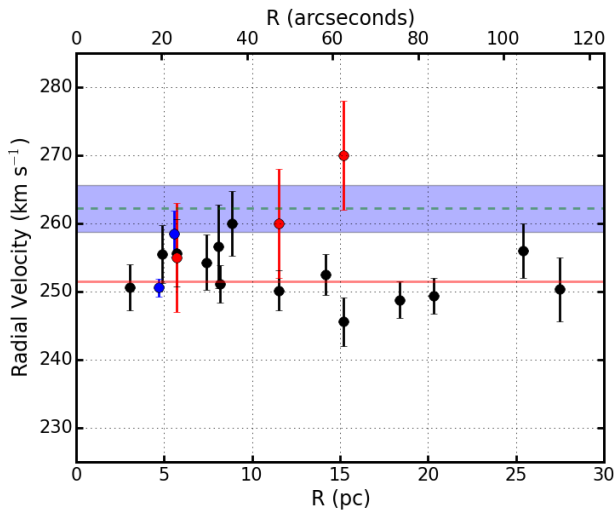
Figure 2. Radial velocities of KMOS targets shown as a function of distance from the cluster centre. Green dashed line shows the LMC systemic velocity with the error highlighted by the blue shaded region (262.2 ± 3.4 km s^{-1}; McConnachie 2012) and the solid red line shows the mean of the sample (251.5 ± 3.4 km s^{-1}). Blue points show the two young stars studied in Evans et al. (2015) and red points show previous estimates for three of the targets (Jasniewicz & Thevenin 1994).

Figure 3. Observed line-of-sight velocity dispersion as a function of the distance from the centre of NGC 2100. The measurement of σ_{1D} includes the radial velocities of all RSGs internal to the target in question. The adopted σ_{1D} from this figure is 3.4 ± 0.4 km s^{-1}.
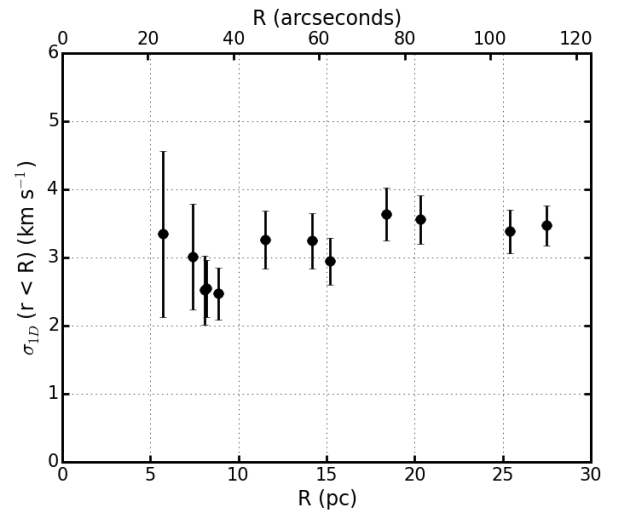
3.2 Velocity Dispersion

An upper limit to the line-of-sight velocity dispersion is calculated using the equations,

$$\mu = \frac{1}{\sum_i 1/\sigma_i^2} \sum_i \frac{RV_i}{\sigma_i}, \qquad (2)$$

$$Var = \frac{1}{\sum_i 1/\sigma_i^2} \sum_i \frac{(RV_i - \mu)^2}{\sigma_i^2}, \qquad (3)$$

$$\sigma_{1D} = \sqrt{Var \frac{N}{N-1}}, \qquad (4)$$

where σ_i is the uncertainty on the radial velocity measurement RV_i, μ is the weighted mean and N is the number of stars in the sample. Figure 3 shows the line-of-sight velocity dispersion profile for RSGs in NGC 2100, where σ_{1D} is calculated for each star using all stars closer to the cluster centre than the star in question. The uncertainties in this figure

are defined as the standard deviation of the radial velocities within the given distance, normalised by the number of measurements in the sample. We see that the dispersion is consistent with a flat profile with a value of ∼3.5 km s^{-1}. The scatter within 10 pc is owing to the low number statistics within this radius. Thus, we adopt $\sigma_{1D} = 3.4 \pm 0.5$ km s^{-1}, where this uncertainty is the average of all the σ_{1D} measurements in Figure 3, as an upper limit on the line-of-sight velocity dispersion profile of NGC 2100. A discussion on how binarity affects this distribution is given in Section 4.2.

Ben's comment:
Did you subtract the measurement error in quadrature first? If you had an intrinsic sigma of zero, but an average error per measurement of e.g. 5kms, then the velocity dispersion you would measure would be ∼5kms and would be dominated by your instrumental errors. To find the 'real' sigma, you need to subtract the measurement error in quadrature.

3.3 Dynamical Mass

Using σ_{1D} as an upper limit on the velocity distribution, one can calculate the dynamical mass of the cluster using the virial equation,

$$M_{dyn} = \frac{\eta \sigma_{1D}^2 r_{eff}}{G},\qquad(5)$$

where M_{dyn} is the virial mass, $\eta = 6r_{vir}/r_{eff} = 9.75$ providing the density profile of the cluster is sufficiently steep (Portegies Zwart et al. 2010). However, NGC 2100 has a relatively shallow density profile ($\gamma = 2.44 \pm 0.14$; Mackey & Gilmore 2003) which means $\eta > 9.75$ and therefore the estimate of M_{dyn} is knowingly an overestimate. Using $\sigma_{1D} = 3.4 \pm 0.5\,\mathrm{km\,s^{-1}}$ and equation 5, the dynamical mass of NGC 2100 is $M_{dyn} = (11.7 \pm 3.3) \times 10^4 M_\odot$. Comparing this to the photometric mass $M_{phot} = (2.3 \pm 1.0) \times 10^4 M_\odot$ (McLaughlin & van der Marel 2005) we see that the dynamical mass appears to be significantly larger. Gieles et al. (2010) explain this discrepancy by demonstrating that binary motions can increase the measured velocity dispersion profile. Hénault-Brunet et al. (2012) noted that had binarity been neglected they would have measured a σ_{1D} a factor of five higher for R136. However, the mean lifetime for RSGs within binary systems is significantly decreased (Eldridge et al. 2008). These authors also noted that where mass transfer occurs, the number of RSGs drastically decreases. We can therefore expect that the numbers of RSGs in close binary systems are very small (Davies et al. 2009). The fraction of RSGs in longer period binary systems is more uncertain, however, these systems would increase the line-of-sight velocity dispersion to a lesser degree.

Assuming that the population of RSGs we observe is entirely single leads to the conclusion that the only factor affecting the estimation of M_{dyn} is the η parameter. Using a lower estimate of $\eta = 7.0$ (estimated from Fig. 4a in Portegies Zwart et al. 2010), $M_{dyn} = (8.4 \pm 2.4) \times 10^4 M_\odot$ cannot account for the discrepancy between the measured masses. However, if the measured line-of-sight velocity dispersion is inflated by binary motions, as discussed in Section 4.2, the measured dynamical mass would be correspondingly increased.

3.4 Stellar Parameters

Stellar parameters are estimated using the *J*-band analysis technique described initially in Davies et al. (2010) and tested rigorously by Gazak et al. (2014) and Davies et al. (2015). These studies show that using a narrow spectral window within the *J*-band one can accurately derive overall metallicities ([Z]) to better than $\pm 0.15\,dex$ at the resolution of KMOS observations with S/N $\geqslant$ 100. Patrick et al. (2015) built on this by demonstrating the feasibility of this technique using KMOS spectra.

The analysis uses synthetic RSG spectra, extracted from MARCS model atmospheres (Gustafsson et al. 2008), computed with corrections for non-local thermodynamic equilibrium for stellar lines from titanium, iron, silicon and magnesium (Bergemann et al. 2012, 2013, 2015). The parameter ranges for the grid of synthetic RSG spectra are listed in Table 3. The synthetic spectra are compared with obser-

Table 3. Model grid used for analysis.

Model Parameter	Min.	Max.	Step size
T_{eff} (K)	3400	4400	100
[Z] (dex)	-1.0	1.0	0.1
$\log g$ (cgs)	-1.00	1.00	0.25
ξ (km s^{-1})	1.0	5.0	0.2

vations using a χ-squared minimisation approach where the synthetic spectra are degraded to the resolution and sampling of the observations.

Estimated stellar parameters are listed in Table 4. Reliable parameters could not be estimated for two stars (J054206.36-691220.2 and J054211.61-691309.2). Figure 4 shows the observed KMOS spectra (black) along with each best-fitting model spectrum (red). The average metallicity for the 14 stars within NGC 2100 is $-0.39 \pm 0.10\,dex$.

The average metallicity in NGC 2100 compares well to estimates of the cluster metallicity using isochrone fitting to the optical colour-magnitude diagram ($-0.34\,dex$; Niederhofer et al. 2015). JT94 reported the only other estimate of stellar metallicity within this cluster, who estimated metallicities using optical spectroscopy of four RSGs. These authors found an average metallicity for NGC 2100 of $-0.32 \pm 0.03\,dex$, which our estimate agrees well with. We find that there are three targets in common with our study: B17, C2, C32 (using the Robertson 1974, nomenclature). **Comparing results we find B17 (J054206.36-691220.2) has a spuriously high metallicity for the sample. However, this spectrum displays no obvious features of a poor telluric correction or sky subtraction with a signal-to-noise ratio far exceeding that of our minimum threshold to perform the analysis.** The results for C2 (J054157.44-691218.1) are consistent with what is reported in JT94, although we note that surface gravity reported here agrees with the estimated photometric surface gravity and the spectroscopic surface gravity in JT94 is significantly lower. In addition we note that the microturblence value quoted in this study is on the edge of the allowed model grid. The results for C32 (J054209.98-691328.8) are consistent with what is reported in JT94, although we note that the best fit microturblence value is at the edge of the model grid.

Using the same analysis technique as in this study, Davies et al. (2015) estimate metallicities for nine RSGs within the LMC, finding an average value of $-0.37 \pm 0.14\,dex$ which our estimate agrees well with.

4 DISCUSSION

4.1 Stellar Parameters

Luminosities have been estimated using the bolometric correction in Davies et al. (2013) and a H-R diagram for the clusters is presented in Figure 5. Overlaid on this H-R diagram are SYCLIST stellar isochrones for SMC-like (solid lines, Georgy et al. 2013) and solar-like (dashed lines, Ekström et al. 2012) models where stellar rotation is 40% of break-up velocity. Even though the temperatures covered by the SMC-like models do not accurately represent the distribu-
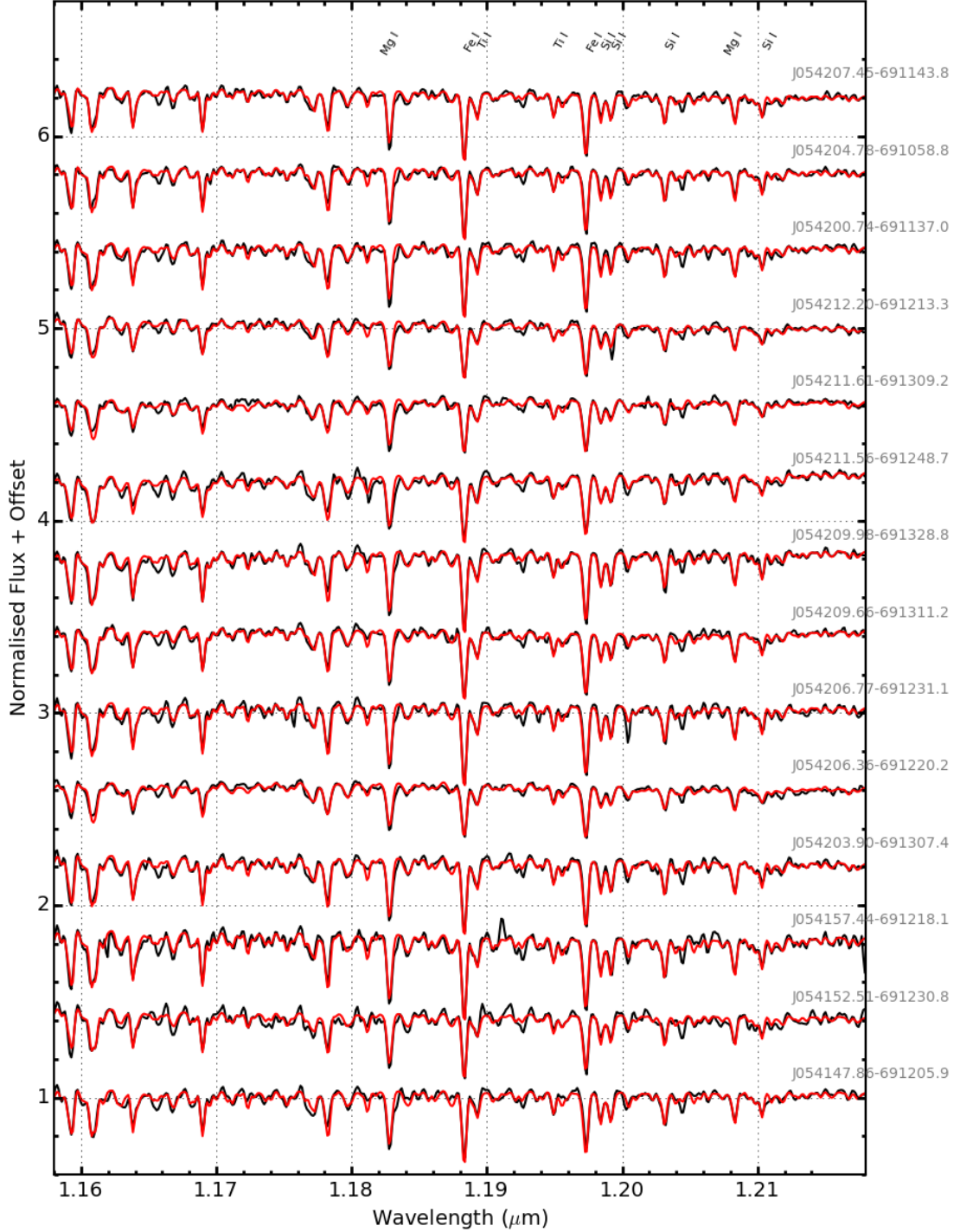
Figure 4. KMOS spectra of the NGC 2100 RSGs and their associated best-fit model spectra (black and red lines, respectively). The lines used for the analysis from left-to-right by species are: Fe I $\lambda\lambda$1.188285, 1.197305, Si I $\lambda\lambda$1.198419, 1.199157, 1.203151, 1.210353, Ti I $\lambda\lambda$1.189289, 1.194954.

Table 4. Physical parameters for the NGC 2100 KMOS targets

Target	IFU	ξ (km s^{-1})	[Z]	$\log g$	T$_{eff}$ (K)	Notes
J054147.86-691205.9	7	3.6 ± 0.19	-0.39 ± 0.07	0.12 ± 0.12	4048 ± 63	
J054152.51-691230.8	9	3.5 ± 0.18	-0.439± 0.09	0.42 ± 0.18	4002 ± 26	
J054157.44-691218.1	6	5.0 ± 0.10	-0.38 ± 0.07	0.18 ± 0.13	3994 ± 43	C2
J054203.90-691307.4	12	4.6 ± 0.14	-0.47 ± 0.05	0.24 ± 0.13	3894 ± 50	
J054206.36-691220.2	24	2.5 ± 0.47	0.01 ± 0.27	0.45 ± 0.11	3773 ± 132	B17
J054206.77-691231.1	10	5.0 ± 0.10	-0.48 ± 0.05	0.24 ± 0.13	3904 ± 50	
J054209.66-691311.2	14	3.7 ± 0.20	-0.34 ± 0.12	0.06 ± 0.21	3767 ± 73	
J054209.98-691328.8	11	5.0 ± 0.10	-0.44 ± 0.09	0.16 ± 0.20	3948 ± 44	C32
J054211.56-691248.7	20	3.8 ± 0.19	-0.21 ± 0.09	-0.01 ± 0.17	3906 ± 68	
J054211.61-691309.2	18	2.1 ± 0.24	0.34 ± 0.08	0.75 ± 0.13	3800 ± 50	
J054212.20-691213.3	22	3.3 ± 0.21	-0.25 ± 0.12	0.36 ± 0.25	4040 ± 54	
J054200.74-691137.0	4	4.2 ± 0.23	-0.44 ± 0.10	0.17 ± 0.10	3784 ± 76	
J054204.78-691058.8	3	4.1 ± 0.20	-0.45 ± 0.09	0.48 ± 0.10	3893 ± 50	
J054207.45-691143.8	2	4.0 ± 0.21	-0.37 ± 0.09	0.48 ± 0.13	3864 ± 50	
NGC 2100 average		4.1 ± 0.58	-0.39 ± 0.08	0.24 ± 0.15	3903 ± 87	
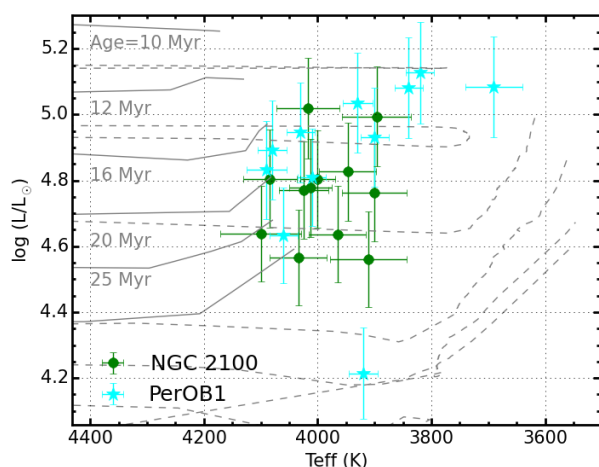
Figure 5. H-R diagram for 12 RSGs in NGC2100. Cluster isochrones for solar (dashed lines; Ekström et al. 2012) and SMC-like (solid lines; Georgy et al. 2013) metal abundances, where stellar rotation is 40% of the break-up velocity, are shown for ages of 10-32 Myr. For comparison, 11 RSGs from the Galactic young massive cluster Perseus OB-1 are overlaid (Gazak et al. 2014).

tion of temperatures observed in this study, it remains useful to fit the data using these models to estimate an age for NGC 2100. The Solar-like models (dashed) demonstrate that increasing the metallicity of the sample a) decreases the temperatures of the RSGs (something which is not observed by Patrick et al. 2015), b) induces a blue-ward evolution for the youngest models and c) decreases the luminosity for the oldest models.

In addition, the blue stars in Figure 5 identify 11 RSGs from the Galactic star cluster Perseus OB-1 (PerOB1; Gazak et al. 2014) where stellar parameters are estimated using the same analysis technique as in this study. PerOB1 is a star cluster with similar mass and age (2×10^4 M$_\odot$ and 14 Myr respectively; Currie et al. 2010) to NGC 2100 and a comparison between the stellar components of these two clusters using a consistent analysis technique can highlight differences in stellar evolution at different metallicities.

We can see from Figure 5 that generally, the two data

sets are in good agreement. The median luminosity for the PerOB1 targets ($10^{4.93\pm0.15}$ L$_\odot$) is slightly above that of NGC 2100 ($10^{4.77\pm0.15}$ L$_\odot$) which could represent the slight difference in ages of the two clusters. As PerOB1 is younger, the average mass for a RSG in the cluster will be larger than the average in NGC 2100. Therefore we would expect to see higher luminosity RSGs in PerOB1. However, the difference between the two samples is barely significant and is consistent with a constant luminosity. The average effective temperature of the two data sets is consistent between the two samples. As Patrick et al. (2015) point out, this is not predicted by evolutionary models. Overall, by comparing these two star clusters with a similar mass, age and stellar population we conclude that there exists no significant difference in appearance on the H-R diagram of RSGs within star clusters of different metallicities.

Davies et al. (2015) estimated stellar parameters for nine RSGs throughout the LMC using the same methodology as in this study. In Figure 6 we compare the effective temperatures and metallicities from NGC 2100 with those derived for RSGs elsewhere in the LMC. We find excellent agreement in the distribution of temperatures from the two studies, with the average agreeing well. The range in [Z] from the LMC population is slightly larger than that of the NGC 2100 RSGs, which is expected when comparing a star cluster with an entire galaxy, however the averages for the two studies agree very well.

4.2 Velocity Dispersion and Dynamical Mass

This study represents the first estimate of the line-of-sight velocity dispersion profile for NGC 2100. Comparing this estimate with that of other young massive clusters in the Local Universe is useful to ascertain whether this cluster shares similar properties to other more well studied young massive clusters. We find the dynamical properties NGC 2100 are well matched by other clusters with similar masses and ages, particularly so with RSGC02, a Galactic young massive cluster. A comparison with a small sample of Local Group YMCs reveals the trend that very young massive clusters have a larger line-of-sight velocity dispersion which relaxes to ~3 km s^{-1} at 10-100 Myr.

As the velocity dispersion estimated in this study is strictly an upper limit to the line-of-sight dispersion, we have
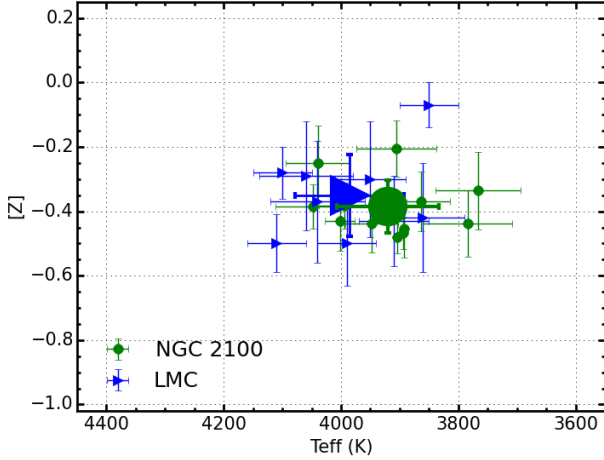
Figure 6. Estimated metallicities for NGC 2100 RSGs in this study shown against effective temperature (green dots). For comparison we show the distribution of LMC RSGs in Davies et al. (blue triangles 2015). This demonstrates the remarkable agreement between the effective temperature ranges and averages for RSGs within these two samples.

to consider the possibility that the dispersion is significantly lower than quoted in this study. This would have the affect of reducing the dynamical mass and potentially bringing it more in line with the quoted photometric mass.

4.3 Simulated Cluster Spectrum Analysis

We can use the individual stars in NGC 2100 to simulate the analysis of a young massive cluster in the more distant Universe using the assumption that RSGs dominate the flux from such a cluster (Gazak et al. 2013). Gazak et al. (2014) use this assumption to create a cluster spectrum for the Galactic star cluster Perseus OB-1 and show that by analysing the combined spectrum from 11 RSGs the resulting parameters are consistent with the average parameters estimated using the individual stars. By reconstrucing the test performed by these authors we can test how metallicity affects this analysis. NGC 2100 has a similar mass and age to Perseus OB-1 with and (Gazak et al. 2014) study a similar number of RSGs to this study, therefore a direct comparison between the two clusters is vaild.

To create the "Cluster Spectrum" we sum all the individual RSG spectra weighted by their *J*-band luminosities. Figure 7 shows the resulting so called Cluster Spectrum. This spectrum is then analysed in the same way described in Section 3.4 for a single RSG. The results of this analysis are what one would expect from KMOS observations of a more-distant young massive cluster where individual stars cannot be resolved. We find a metallicity of $-0.32 \pm 0.11\,dex$, effective temperature of $3953 \pm 49\,K$, surface gravity of $0.34 \pm 0.23\,dex$ and a microturblence velocity of $3.8 \pm 0.2\,km\,s^{-1}$ which agree well with the average of the individual RSG parameters.

5   CONCLUSIONS

Using KMOS spectra of 14 RSGs in NGC 2100 we have for the first time estimated the dynamical properties of this young massive cluster. Radial velocities have been estimated using KMOS, to a precision of $\sim 1\,km\,s^{-1}$, demonstrating that this instrument can be used to study the dynamical properties of star clusters in external galaxies.

The line-of-sight velocity dispersion profile has been estimated in Figure 3 and has been shown to be flat outside 10 pc from the cluster centre. A low velocity dispersion of $\sigma_{1D} = 3.4 \pm 0.5\,km\,s^{-1}$ has been adopted and NGC 2100 has therefore been shown to be in virial equilibrium. This adds evidence to the theory that young star clusters appear to remain in virial equilibrium from an early age and hence expand owing to stellar evolution on a relatively slow timescale (10 Myr Portegies Zwart et al. 2010). We compare the velocity dispersion profile estimated here to that of other young massive clusters in the LMC and the Galaxy and find that the distribution of velocity dispersions is consistent with this expansion.

Characterisation of the velocity dispersion profile for the cluster allows for the first time the dynamical mass to be estimated (assuming virial equilibrium) as $M_{dyn} = (11.7 \pm 3.3) \times 10^4 M_{\odot}$. A discussion of the appropriate value of η for this cluster is detailed in Section 3.3.

In addition to estimating the dynamical properties of this star cluster we have also reliably estimated stellar parameters for 12 RSGs in NGC 2100 using the new *J*-band analysis technique (Davies et al. 2010). We find the average metallicity for RSGs in NGC 2100 is $-0.39 \pm 0.10\,dex$, which agrees well with previous studies within this cluster.

The H-R diagram of NGC 2100 is compared with that of PerOB1: a Galactic young massive cluster with a similar age, mass and stellar population. Using stellar parameters estimated from 11 RSGs using the same analysis technique as that in this study, we demonstrate that there exists no significant difference in the appearance of the H-R diagram of YMCs between Solar- and LMC-like metallicities.

Using the H-R diagram we have estimated the age of the cluster using isochrones fitting (Ekström et al. 2012; Georgy et al. 2013) to be $20 \pm 5\,Myr$, in good agreement with the estimate for this cluster from Niederhofer et al. (2015).

By combining the individual RSG spectra within NGC 2100, we have created an integrated "Cluster Spectrum" and proceeded to analyse this spectrum using the same techniques for that of the individual RSGs, as RSGs dominate the cluster light in the *J*-band (Gazak et al. 2013). The results of this technique demonstrate the potential of this analysis for integrated light spectra of more distant young massive clusters in low-metallicitiy environments. We find good agreement using the "Cluster Spectrum" with the average results of the individual RSGs.
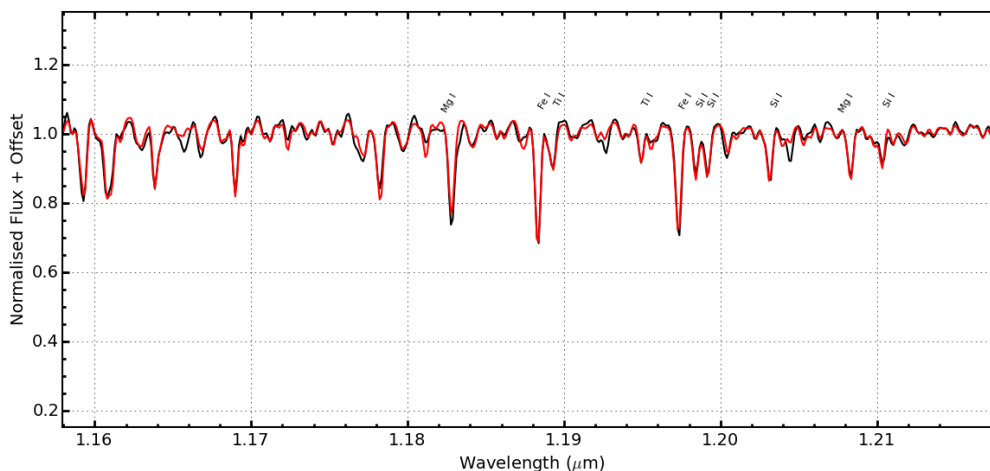
Figure 7. Combined "Cluster Spectrum" as a result of adding the individual RSG spectra weighted by their *J*-band luminosities. Shown in red is the best fit model spectrum.

REFERENCES

Andrews, P. J., & Lloyd Evans, T. 1972, MNRAS, 159, 445

Banerjee, S., & Kroupa, P. 2013, ApJ, 764, 29

Banerjee, S., & Kroupa, P. 2015, arXiv:1512.03074

Bergemann, M., Kudritzki, R.-P., Plez, B., et al. 2012, ApJ, 751, 156

Bergemann, M., Kudritzki, R.-P., Würl, M., et al. 2013, ApJ, 764, 115

Bergemann, M., Kudritzki, R.-P., Gazak, Z., Davies, B., & Plez, B. 2015, ApJ, 804, 113

Clark, J. S., Negueruela, I., Crowther, P. A., & Goodwin, S. P. 2005, A&A, 434, 949

Crowther, P. A., Schnurr, O., Hirschi, R., et al. 2010, MN-RAS, 408, 731

Currie, T., Hernandez, J., Irwin, J., et al. 2010, ApJS, 186, 191

Davies, B., Figer, D. F., Kudritzki, R.-P., et al. 2007, ApJ, 671, 781

Davies, B., Origlia, L., Kudritzki, R.-P., et al. 2009, ApJ, 696, 2014

Davies, B., Kudritzki, R.-P., & Figer, D. F. 2010, MNRAS, 407, 1203

Davies, B., Kudritzki, R.-P., Plez, B., et al. 2013, ApJ, 767, 3

Davies, B., Kudritzki, R.-P., Gazak, Z., et al. 2015, ApJ, 806, 21

Davies, R. I., Agudo Berbel, A., Wiezorrek, E., et al. 2013, A&A, 558, A56

de Koter, A., Heap, S. R., & Hubeny, I. 1998, ApJ, 509, 879

de Wit, W. J., Testi, L., Palla, F., & Zinnecker, H. 2005, A&A, 437, 247

Ekström, S., Georgy, C., Eggenberger, P., et al. 2012, A&A, 537, A146

Eldridge, J. J., Izzard, R. G., & Tout, C. A. 2008, MNRAS, 384, 1109

Elson, R. A. W. 1991, ApJS, 76, 185

Evans, C. J., Lennon, D. J., Smartt, S. J., & Trundle, C. 2006, A&A, 456, 623

Evans, C. J., Taylor, W. D., Hénault-Brunet, V., et al. 2011, A&A, 530, A108

Evans, C. J., van Loon, J. T., Hainich, R., & Bailey, M. 2015, arXiv:1508.03490

Ford, H., 1970, PhD. Thesis, University of Wisconsin.

Freeman, K. C., Illingworth, G., & Oemler, A., Jr. 1983, ApJ, 272, 488

Gazak, J. Z., Bastian, N., Kudritzki, R.-P., et al. 2013, MNRAS, 430, L35

Gazak, J. Z., Davies, B., Kudritzki, R., Bergemann, M., & Plez, B. 2014, ApJ, 788, 58

Gazak, J. Z., Davies, B., Bastian, N., et al. 2014, ApJ, 787, 142

Gazak, J. Z., Kudritzki, R., Evans, C., et al. 2015, ApJ, 805, 182

Georgy, C., Ekström, S., Eggenberger, P., et al. 2013, A&A, 558, A103

Gieles, M., Sana, H., & Portegies Zwart, S. F. 2010, MN-RAS, 402, 1750

Gratton, R. G., Lucatello, S., Carretta, E., et al. 2012, A&A, 539, A19

Gustafsson, B., Edvardsson, B., Eriksson, K., et al. 2008, A&A, 486, 951

Hénault-Brunet, V., Evans, C. J., Sana, H., et al. 2012, A&A, 546, A73

Jasniewicz, G., & Thevenin, F. 1994, A&A, 282, 717

King, I. R. 1966, AJ, 71, 64

Lada, C. J., & Lada, E. A. 2003, ARA&A, 41, 57

Lapenna, E., Origlia, L., Mucciarelli, A., et al. 2015, ApJ, 798, 23

Longmore, S. N., Kruijssen, J. M. D., Bastian, N., et al. 2014, Protostars and Planets VI, 291

Mackey, A. D., & Gilmore, G. F. 2003, MNRAS, 338, 85

Massey, P., & Hunter, D. A. 1998, ApJ, 493, 180

McConnachie, A. W. 2012, AJ, 144, 4

McLaughlin, D. E., & van der Marel, R. P. 2005, ApJS, 161, 304

Miller, B. W., Whitmore, B. C., Schweizer, F., & Fall, S. M. 1997, AJ, 114, 2381

Niederhofer, F., Hilker, M., Bastian, N., & Silva-Villa, E.

2015, A&A, 575, A62

Parker, R. J., & Goodwin, S. P. 2007, MNRAS, 380, 1271

Patrick, L. R., Evans, C. J., Davies, B., et al. 2015, ApJ, 803, 14

Points, S. D., Chu, Y. H., Kim, S., et al. 1999, ApJ, 518, 298

Portegies Zwart, S. F., McMillan, S. L. W., & Gieles, M. 2010, ARA&A, 48, 431

Robertson, J. W. 1974, A&AS, 15, 261

Sana, H., de Mink, S. E., de Koter, A., et al. 2012, Science, 337, 444

Sharples, R., Bender, R., Agudo Berbel, A., et al. 2013, The Messenger, 151, 21

Smith, M. G., & Weedman, D. W. 1971, ApJ, 169, 271

Whitmore, B. C., & Schweizer, F. 1995, AJ, 109, 960

Zepf, S. E., Ashman, K. M., English, J., Freeman, K. C., & Sharples, R. M. 1999, AJ, 118, 752